THE GEOMETRY OF THE INFRARED AND X-RAY OBSCURER IN A DUSTY HYPERLUMINOUS QUASAR

DUNCAN FARRAH[1], MISLAV BALOKOVIĆ[2], DANIEL STERN[3], KATHRYN HARRIS[1,4,5], MICHELLE KUNIMOTO[6], DOMINIC J. WALTON[3],
DAVID M. ALEXANDER[7], PATRICIA ARÉVALO[8], DAVID R. BALLANTYNE[9], FRANZ E. BAUER[10,11,12,13], STEVEN BOGGS[14],
WILLIAM N. BRANDT[15,16,17], MURRAY BRIGHTMAN[2], FINN CHRISTENSEN[18], DAVID L. CLEMENTS[6], WILLIAM CRAIG[13,19],
ANDREW FABIAN[20], CHARLES HAILEY[21], FIONA HARRISON[2], MICHAEL KOSS[22], GEORGE B. LANSBURY[7], BIN LUO[23,24],
JENNIE PAINE[1], SARA PETTY[25], KATE PITCHFORD[1], CLAUDIO RICCI[10,13], AND WILLIAM ZHANG[26]

[1] Department of Physics, Virginia Tech, Blacksburg, VA 24061, USA; farrah@vt.edu
[2] Cahill Center for Astronomy and Astrophysics, California Institute of Technology, Pasadena, CA 91125, USA
[3] Jet Propulsion Laboratory, California Institute of Technology, Pasadena, CA 91109, USA
[4] Instituto de Astrofisica de Canarias (IAC), E-38200 La Laguna, Tenerife, Spain
[5] Departamento de Astrofisica, Universidad de La Laguna (ULL), E-38205 La Laguna, Tenerife, Spain
[6] Astrophysics Group, Imperial College London, Blackett Laboratory, Prince Consort Road, London SW7 2AZ, UK
[7] Department of Physics, Durham University, Durham DH1 3LE, UK
[8] Instituto de Física y Astronomía, Facultad de Ciencias, Universidad de Valparaíso, Gran Bretana N 1111, Playa Ancha, Valparaíso, Chile
[9] Center for Relativistic Astrophysics, School of Physics, Georgia Institute of Technology, 837 State Street, Atlanta, GA 30332-0430, USA
[10] Instituto de Astrofísica, Facultad de Física, Pontificia Universidad Católica de Chile, Casilla 306, Santiago 22, Chile
[11] Millennium Institute of Astrophysics, MAS, Nuncio Monseñor Sótero Sanz 100, Providencia, Santiago de Chile
[12] Space Science Institute, 4750 Walnut Street, Suite 205, Boulder, CO 80301, USA
[13] EMBIGGEN Anillo, Concepción, Chile
[14] Space Science Laboratory, University of California, Berkeley, CA 94720, USA
[15] Department of Astronomy & Astrophysics, 525 Davey Lab, The Pennsylvania State University, University Park, PA 16802, USA
[16] Institute for Gravitation and the Cosmos, The Pennsylvania State University, University Park, PA 16802, USA
[17] Department of Physics, 104 Davey Lab, The Pennsylvania State University, University Park, PA 16802, USA
[18] DTU Space, National Space Institute, Technical University of Denmark, Elektrovej 327, DK-2800 Lyngby, Denmark
[19] Lawrence Livermore National Laboratory, Livermore, CA 94550, USA
[20] Institute of Astronomy, Madingley Road, Cambridge, CB3 0HA, UK
[21] Physics Department, Columbia University, New York, NY 10027, USA
[22] Institute for Astronomy, Department of Physics, ETH Zurich, Wolfgang-Pauli-Strasse 27, CH-8093 Zurich, Switzerland
[23] School of Astronomy and Space Science, Nanjing University, Nanjing, 210093, China
[24] Key laboratory of Modern Astronomy and Astrophysics (Nanjing University), Ministry of Education, Nanjing 210093, China
[25] Green Science Policy Institute, Berkeley, CA 94709, USA
[26] NASA Goddard Space Flight Center, Greenbelt, MD 20771, USA

ABSTRACT

We study the geometry of the active galactic nucleus (AGN) obscurer in IRAS 09104+4109, an IR-luminous, radio-intermediate FR-I source at $z = 0.442$, using infrared data from *Spitzer* and *Herschel*, X-ray data from *NuSTAR*, *Swift*, *Suzaku*, and *Chandra*, and an optical spectrum from Palomar. The infrared data imply a total rest-frame 1–1000 μm luminosity of 5.5×10^{46} erg s^{-1} and require both an AGN torus and a starburst model. The AGN torus has an anisotropy-corrected IR luminosity of 4.9×10^{46} erg s^{-1} and a viewing angle and half-opening angle both of approximately 36° from pole-on. The starburst has a star formation rate of $(110 \pm 34) M_\odot$ yr^{-1} and an age of <50 Myr. These results are consistent with two epochs of luminous activity in IRAS 09104+4109: one approximately 150 Myr ago, and one ongoing. The X-ray data suggest a photon index of $\Gamma \simeq 1.8$ and a line-of-sight column density of $N_H \simeq 5 \times 10^{23}$ cm^{-2}. This argues against a reflection-dominated hard X-ray spectrum, which would have implied a much higher N_H and luminosity. The X-ray and infrared data are consistent with a bolometric AGN luminosity of $L_{bol} \sim (0.5–2.5) \times 10^{47}$ erg s^{-1}. The X-ray and infrared data are further consistent with coaligned AGN obscurers in which the line of sight "skims" the torus. This is also consistent with the optical spectra, which show both coronal iron lines and broad lines in polarized but not direct light. Combining constraints from the X-ray, optical, and infrared data suggest that the AGN obscurer is within a vertical height of 20 pc, and a radius of 125 pc, of the nucleus.

Key words: galaxies: evolution – galaxies: individual (IRAS 09104+4109) – galaxies: Seyfert – galaxies: starburst – infrared: galaxies – X-rays: galaxies

1. INTRODUCTION

A significant fraction of galaxy assembly at $z \gtrsim 0.5$ proceeds via episodes of rapid star formation (hundreds to thousands of solar masses per year) and accretion onto supermassive black holes at a non-negligible fraction of the Eddington limit (e.g., Lilly et al. 1996; Dickinson et al. 2003; Pérez-González et al. 2005; Farrah et al. 2008; Wuyts et al. 2011; Alexander & Hickox 2012; Béthermin et al. 2012; Madau & Dickinson 2014; Rowan-Robinson et al.

2016). Moreover, there is evidence for a deep connection between starburst and active galactic nucleus (AGN) activity at all redshifts, from, for example, the $M_{bh}-\sigma$ relation (e.g., Magorrian et al. 1998; Tremaine et al. 2002), and from the presence of starbursts and AGNs in the same systems (Genzel et al. 1998; Farrah et al. 2003; Alexander et al. 2005; Lonsdale et al. 2006, p. 285, Hernán-Caballero et al. 2009; Harris et al. 2016) at rates much higher than expected by chance. There is also evidence that star formation and AGN activity can

directly affect each other (see Fabian 2012 for a review), via both quenching (e.g., Croton et al. 2006; Chung et al. 2011; Farrah et al. 2012; Alatalo et al. 2015; Schaye et al. 2015) and triggering (e.g., King 2005; Gaibler et al. 2012; Ishibashi & Fabian 2012; Silk 2013; Zubovas et al. 2013).

The connection between star formation and AGN activity is challenging to study, for two reasons. First, the bulk of these activities occur at high redshifts, $1 \lesssim z \lesssim 7$ (e.g., Chapman et al. 2005; Richards et al. 2006; Wang et al. 2013; Delvecchio et al. 2014), where they are seen both faintly and at coarsened spatial scales. Second, star-forming regions and AGNs are often occulted by large column densities of gas and dust. Thus, a substantial fraction of their light is observed in the infrared (Alexander et al. 2005; Lagache et al. 2005; Iglesias-Páramo et al. 2007; Bridge et al. 2013; Burgarella et al. 2013; Farrah et al. 2013; Mignoli et al. 2013; Casey et al. 2014; Vignali et al. 2014; Lanzuisi et al. 2015; Gruppioni et al. 2016). A choate picture of how star formation and AGN activity contribute to galaxy assembly thus requires both deep and wide blank-field extragalactic surveys and case studies of individual objects at lower redshifts. The latter serve to create archetypes at high sensitivity and spatial resolution for how star formation and AGN activity proceed in galaxies, and to illustrate how constraints from multiwavelength data can be combined.

IRAS 09104+4109 (Kleinmann et al. 1988) at $z = 0.442$ (Hewett & Wild 2010) is one such archetype, for the relationship between luminous, obscured AGNs and star formation. In the radio it is a "radio-intermediate" FR-I source, with a linear core and double-lobed structure (Hines & Wills 1993; O'Sullivan et al. 2012). It is extremely IR-luminous (Rowan-Robinson 2000; Ruiz et al. 2010; Vignali et al. 2011) with a rest-frame 1–1000 μm luminosity of $\sim 4 \times 10^{46}$ erg s^{-1}, of which at least 70% arises from AGN activity. The mass of free baryons in the system is, however, small compared to other IR-luminous systems, with only $\sim 3.2 \times 10^9 M_\odot$ of molecular hydrogen and of order $10^7 M_\odot$ of warm dust (Evans et al. 1998; Combes et al. 2011). Its optical spectrum is that of an Sy2 (Kleinmann et al. 1988; Soifer et al. 1996; Véron-Cetty & Véron 2006), but with broad Hβ, Hγ, and Mg II lines in polarized light (Hines & Wills 1993; Tran et al. 2000). There is also a polarized, bipolar reflection nebula centered on the nucleus (Hines et al. 1999). Its optical spectrum further reinforces its extreme nature; for example, its [O III] $\lambda 5007$ luminosity, at 7.7×10^{43} erg s^{-1}, is nearly an order of magnitude higher than any other type 2 quasar at $z < 0.5$ (Lansbury et al. 2015). Inferring a current star formation rate from the EW of [O II] $\lambda 3727$ yields $41 \pm 12 M_\odot$ yr^{-1} (Bildfell et al. 2008). There is also evidence, from fitting model star formation histories to UV through optical photometry, for an episode of star formation 100–200 Myr ago (Pipino et al. 2009). Optical imaging and integral field spectroscopy reveal a disturbed system with several bright "knots" within its stellar envelope, of which one may be a second nucleus, multiple companions within 100 kpc, and extended, [O III] bright filaments (Crawford & Vanderriest 1996; Soifer et al. 1996; Armus et al. 1999).

IRAS 09104+4109 is a cD galaxy within the rich cluster MACS J0913.7+4056 (Kleinmann et al. 1988; Hall et al. 1997; Farrah et al. 2004). This cluster is associated with spatially extended X-ray emission with a strong cool core (Fabian & Crawford 1995; Crawford & Vanderriest 1996). Other examples of cool-core clusters hosting powerful AGNs at

$z < 1$ are known, including H1821+643 (Russell et al. 2010) and the Phoenix cluster (McDonald et al. 2015). Two cavities are visible in the X-ray emission, coincident with the radio hot spots (Hlavacek-Larrondo et al. 2012). IRAS 09104+4109 itself is luminous in the X-ray (Fabian et al. 1994). The soft X-ray emission is dominated by plasma with a temperature of ~ 5 keV (e.g., Franceschini et al. 2000; O'Sullivan et al. 2012). A hard component starts to contribute above 5 keV and dominates above 8 keV. Two origins have been proposed for the hard component: the intrinsic AGN continuum transmitted along a line of sight absorbed by a column density of $\sim 5 \times 10^{23}$ cm^{-2}, or reflection from cold material surrounding the X-ray source. The latter possibility requires a Compton-thick column density ($\gtrsim 5 \times 10^{24}$ cm^{-2}) along the line of sight in order to completely obscure the intrinsic continuum. The X-ray-based determination of the intrinsic luminosity depends on which of these two scenarios dominates (e.g., Franceschini et al. 2000; Iwasawa et al. 2001; Piconcelli et al. 2007; Vignali et al. 2011; Chiang et al. 2013; LaMassa et al. 2014).

Other than being an example of a key phase in AGN evolution, IRAS 09104+4109 is an excellent candidate for being the most luminous Compton-thick quasar at $z \lesssim 0.5$. It may thus be one of the few Compton-thick objects that is bright enough for probing the obscurer structure at multiple wavelengths, from the infrared (IR) through X-ray. A larger sample of luminous obscured quasars at $0.1 < z < 0.5$ (all of which are at least a factor of ~ 5 less luminous than IRAS 09104+4109) has been studied with *NuSTAR* by Lansbury et al. (2014, 2015), in addition to single-object studies at lower ($z = 0.051$; Gandhi et al. 2014) and higher redshift ($z \approx 2$; Del Moro et al. 2014). All targets in the *NuSTAR* survey of type 2 quasars have been found to have either Compton-thick obscuration or high obscuration with column densities in the 10^{23}–10^{24} cm^{-2} range. While short *NuSTAR* observations typically yield only weak detections of these sources, several have sufficient photon statistics for modeling the obscurer in detail. Together with IRAS 09104+4109, they form a small but important sample of high-luminosity AGNs that bridge the gap between well-studied AGNs in the local universe (e.g., Brightman et al. 2015) and their counterparts at high redshift (e.g., Iwasawa et al. 2005; Stern et al. 2014).

This system has thus been the subject of several multi-wavelength studies (e.g., Vignali et al. 2011). In this paper we combine a new X-ray observation from *NuSTAR* and a new optical spectrum from Palomar with all available archival X-ray and IR data to study both the geometry of the AGN obscurer and current star formation in IRAS 09104+4109. We constrain the viewing angle, torus opening angle, and other geometric properties of the IR- and X-ray-emitting AGN obscurer and clearly detect ongoing star formation in the host galaxy. We adopt a position for IRAS 09104+4109 of $09^h13^m45\overset{s}{.}49$, $+40^d56^m28\overset{s}{.}22$ (J2000) and assume $H_0 = 70$ km s^{-1} Mpc^{-1}, $\Omega = 1$, and $\Omega_\Lambda = 0.7$. We quote all luminosities in units of erg s^{-1}.

2. OBSERVATIONS

2.1. Infrared and Optical

We assembled IR data from several sources. Photometry at 3.6 and 5.8 μm from the Infrared Array Camera (IRAC; Fazio et al. 2004) on board *Spitzer* (Werner et al. 2004) was obtained from Ruiz et al. (2010) and checked against the *WISE* public

Table 1
Assembled Infrared Photometry of IRAS 09104+4109

Facility	Wavelength (μm)	Flux Density (mJy)
Spitzer-IRAC	3.6	4.74 ± 1.21
Spitzer-IRAC	5.8	26.4 ± 7.11
Herschel-PACS	70	439 ± 24
Herschel-PACS	100	319 ± 18
Herschel-PACS	160	160 ± 23
Herschel-SPIRE	250	72 ± 14
Herschel-SPIRE	350	<50
Herschel-SPIRE	500	<50
JCMT-SCUBA	850	<10

Note. The IR data also include the *Spitzer*-IRS spectrum in Figure 1. The PACS flux density errors include uncertainties arising from celestial standard models (Balog et al. 2014). Upper limits are quoted at 3σ significance.

catalogs (Wright et al. 2010; Cutri et al. 2013). A spectrum from the Infrared Spectrograph (IRS; Houck et al. 2004) on *Spitzer*, spanning observed-frame 6–34 μm, was acquired from version LR6 of the Cornell Atlas of *Spitzer*/IRS Sources (CASSIS; Lebouteiller et al. 2011). The spectrum (AOR key 6619136) was taken in cycle 3 of *Spitzer* operations. The calibration of these data was checked against published *Spitzer* IRAC and MIPS data (Ruiz et al. 2010) and against *WISE*. Photometry at 70, 100, and 160 μm was obtained from archival observations by the Photodetector Array Camera and Spectrometer (PACS; Poglitsch et al. 2010) on board *Herschel* (Pilbratt et al. 2010). The raw data were reduced with version 14 of the *Herschel* Interactive Processing Environment (HIPE; Ott 2010), and flux densities were extracted using aperture photometry within HIPE. The 70 and 100 μm data were checked for consistency against the 60 and 100 μm data from the *Infrared Astronomical Satellite* (*IRAS*; Neugebauer et al. 1984), from both Wang & Rowan-Robinson (2010) and manual reprocessing of the *IRAS* data using the Scan Processing and Integration tool (SCANPI). Photometry at 250, 350, and 500 μm was obtained from archival observations by the Spectral and Photometeric Imaging REceiver instrument (SPIRE; Griffin et al. 2010) on board *Herschel* and processed within HIPE. Finally, an 850 μm flux density was obtained from Deane & Trentham (2001). The photometry flux densities are presented in Table 1. The IRS spectrum is presented in Ruiz et al. (2013) and in the SED plot, where it is plotted as multiple photometric points.

Some IR data are not included in this compilation. We do not include data from *WISE* or *IRAS* since the *Spitzer* and *Herschel* data cover their wavelengths at higher sensitivity and improved spectral resolution. We also do not include data at wavelengths shortward of 3.6 μm. Our aim is to constrain the properties of the obscured AGN (in particular the geometry of the obscurer) and any ongoing star formation (see Section 3). The integrated emission from older stars is almost certainly negligible at observed-frame wavelengths of 3.6 μm and longer, but may contribute significantly at shorter wavelengths.

We obtained an optical spectrum of IRAS 09104+4109 on UT 2014 December 23 using the Double Spectrograph (DBSP; Oke & Gunn 1982), a dual-beam spectrograph on the 5 m Hale Telescope at Palomar Observatory. Our spectrum complements that presented in Tran et al. (2000); their spectrum was taken in 112 minutes using LRIS on Keck and

so is deeper, but our spectrum extends ∼700 Å further redward and was taken closer in time to the X-ray data. The night was photometric, albeit with 2″ seeing. We observed IRAS 09104+4109 for 500 s, split into two equal exposures. We used the 5500 Å dichroic, the 2″ wide long slit, the $600\,\ell\,\mathrm{mm}^{-1}$ grating on the blue arm of the spectrograph (blazed at 4000 Å; resolving power $R \equiv \lambda/\Delta\lambda \sim 900$), and the $316\,\ell\,\mathrm{mm}^{-1}$ grating on the red arm of the spectrograph (blazed at 7500 Å; $R \sim 1200$). The data were processed using standard procedures within the Image Reduction and Analysis Facility (IRAF) environment. Flux calibration was calculated using observations of standard stars Feige 66 and Feige 110 from Massey & Gronwall (1990), obtained on the same night.

2.2. X-Ray

IRAS 09104+4109 was observed with *NuSTAR* (Harrison et al. 2013) on 2012 December 26 with a total exposure of 15.2 ks (OBSID 60001067) as part of the *NuSTAR* program to observe type 2 QSOs (Lansbury et al. 2014, 2015). The observation was coordinated with the *Swift* observatory, which observed the same target on 2012 December 25 (OBSID 00080413001). The total *Swift*/XRT exposure was 6.0 ks. The *NuSTAR* and *Swift* observations are sufficiently close in time that they provide a quasi-simultaneous snapshot of IRAS 09104+4109 across the broad 0.5–70 keV band. This observing strategy is typical for the *NuSTAR* snapshot survey of AGNs in the nearby universe (M. Baloković et al. 2016, in preparation). The *Swift* and *NuSTAR* data are presented here for the first time. All observations used in this paper are listed in Table 2.

The *NuSTAR* data were reduced in the manner described in Perri et al. (2014). We used HEASOFT v6.16, NuSTARDAS v1.4.1, and CALDB version 20150316, with a 50″ extraction radius. Following the event filtering, we extracted the source spectrum from a circular aperture centered on the peak of the point source. The background extraction region covered the free area of the same detector, excluding a region of ≃80″ radius around the source. The target is detected in the 10–50 keV band with a signal-to-noise ratio of ≃10 in FPMA and ≃8 in FPMB. The 10–50 keV (3–79 keV) background-subtracted count rates are $0.010\,\mathrm{s}^{-1}$ ($0.034\,\mathrm{s}^{-1}$) and $0.008\,\mathrm{s}^{-1}$ ($0.032\,\mathrm{s}^{-1}$). The spectrum and corresponding response files were generated using the `nuproducts` script. Spectra for each *NuSTAR* module are binned to a minimum of 20 counts per bin and fitted simultaneously as described in Section 4. We allowed the cross-normalization factor to vary in all fits (with instrumental normalization of FPMA fixed at unity) and found it to be consistent with unity to within 5% in all cases.

We used resources provided by the ASDC[27] for *Swift*/XRT data reduction. The spectrum was extracted from a region with a radius of 20″ centered on the brightest peak of emission, and the background was sampled from an annulus extending between 40″ and 80″ around the source. For spectral fitting we used the source spectrum binned to a minimum of 20 counts per bin before background subtraction. The *Swift* data photon statistics are well matched to those of the *NuSTAR* data.

We complement these data with archival X-ray data taken with *Suzaku* on 2011 November 18 (OBSID 706038010; 81 ks) and with *Chandra* on 2009 January 6 (OBSID 10445; 69 ks). We largely followed the processing steps of Chiang

---

[27] http://www.asdc.asi.it/mmia/

et al. (2013) for these data sets in order to facilitate a direct comparison of the results, so we refer the reader to their data section for details. The *Suzaku* data were reduced using standard procedures.[28] No detection was achieved with the HXD/PIN, so we only made use of the soft X-ray data. The spectra were extracted from circular regions $100''$ in radius, which includes most of the diffuse emission. Background spectra were extracted from emission-free areas of each XIS detector. The spectra from the two front-illuminated chips (XIS0 and XIS3) were coadded. We binned the spectra to a minimum signal-to-noise ratio of 3 and ignored any data outside of the 0.5–8.5 keV range.

The *Chandra* data were processed using CIAO version 4.6. We extracted the nuclear spectrum from a circular region $1''$ in radius centered on the peak of the emission. Background was sampled from a ring with an inner radius of $2''$ and an outer radius of $4''$; in this way most ($\gtrsim 90\%$) of the diffuse emission contribution to the unresolved central source is removed. Unlike all other instruments used in this work, which sample both the AGN and diffuse emission on $\sim 10''$ scales, *Chandra* allows us to isolate the AGN-dominated core emission. In order to assess the contribution of diffuse emission in *NuSTAR* and *Suzaku* apertures, we also extracted *Chandra* spectra from circular regions with $50''$ and $100''$ radii. These extractions are used only in the comparison between instruments presented in Section 4.4.

3. INFRARED AND OPTICAL ANALYSIS

We assume that the IR emission arises from a single episode of star formation and/or AGN activity. We then fit the IR data simultaneously with two grids of precomputed radiative transfer models: one for dusty AGNs (Efstathiou & Rowan-Robinson 1995; Efstathiou et al. 2013) and one for starbursts (Efstathiou et al. 2000). A model set for old stellar populations is not included, for the reasons given in Section 2.1. These models have been used previously in, e.g., Verma et al. (2002), Farrah et al. (2002, 2003, 2012), and Efstathiou et al. (2013). The AGN models assume that the dust geometry is a smooth tapered disk whose height, h, increases linearly with distance, r, from the AGN until it reaches a constant value. The dust distribution includes multiple species of varying sizes and assumes that the density distribution scales as r^{-1}. The AGN model parameters are as follows: inner half-opening angle of the torus measured from pole-on ($15°$–$60°$), viewing angle measured from pole-on ($1°$–$90°$), ratio of inner to outer disk radius ($r_1/r_2 = 0.00625$–0.05), ratio of height to outer radius ($h/r_2 = 0.0625$–0.5), and equatorial optical depth at 1000 Å (250 to 1250, defined in Equations (1) and (2) of Efstathiou & Rowan-Robinson 1995; see also Efstathiou & Rowan-Robinson 1990). The starburst models combine the stellar population synthesis code of Bruzual & Charlot (2003) with a prescription for radiative transfer through dust that includes the effects of small dust grains and polycyclic aromatic hydrocarbons (PAHs) updated with the dust model of Efstathiou & Siebenmorgen (2009). The starburst model parameters are age (0–70 Myr), initial optical depths of the molecular clouds ($\tau_V = 50$, 75, and 100), and e-folding timescale for the starburst (10–40 Myr). In total there are 1680 starburst models and 4212 AGN models.
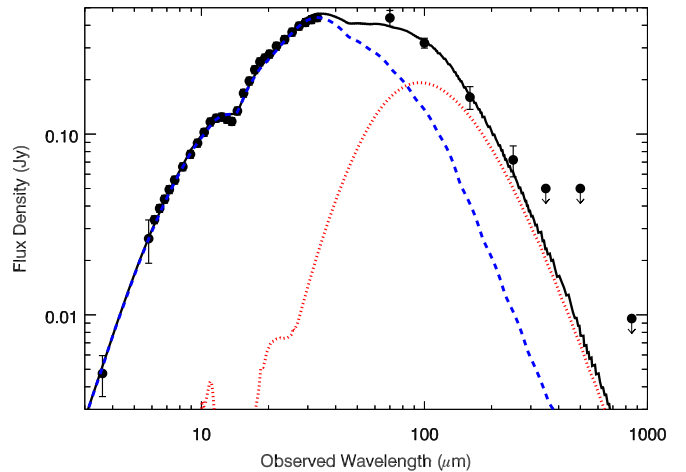
**Figure 1.** Best-fit ($\chi^2_{\rm red} = 0.7$) IR spectral energy distribution for IRAS 09104 +4109. The black line is the combined model, the blue line is the AGN, and the red line is the starburst. The data include IRAC photometry, IRS spectroscopy (see also Sargsyan et al. 2008; Zakamska et al. 2008; Shan & Chen 2012; Ruiz et al. 2013), and PACS, SPIRE, and SCUBA photometry.

The best-fit IR SED is shown in Figure 1. The total IR (rest-frame 1–1000 μm) luminosity is $(6.76 \pm 0.20) \times 10^{46}$ erg s^{-1}, with a contribution from the AGNs of $5.94^{+0.26}_{-0.27} \times 10^{46}$ erg s^{-1}. The starburst is required in the fit at 3.7σ confidence, with a luminosity of $(5.54 \pm 1.48) \times 10^{45}$ erg s^{-1}, corresponding to a star formation rate of $(110^{+35}_{-28}) M_\odot$ yr^{-1}. The uncertainties on these parameters are the 68% confidence intervals, evaluated using the method in Farrah et al. (2012).

The combination of a mid-IR spectrum with far-IR photometry allows constraints to be set on other model parameters. Since the IR data are, however, still relatively limited, we have deduced these constraints by considering all the individual solutions in weighted probability distribution functions, and so we do not consider how these constraints may depend on each other. We have also not explored how these constraints depend on the choice of model set. In particular, we have not explored how these constraints may change if a clumpy, rather than smooth, dust distribution is assumed. With these caveats in mind, we present the following results. The starburst age is constrained (at 3σ) to be <50 Myr. The line-of-sight viewing angle, $\theta^{\rm ir}_{\rm V}$, to the IR-emitting torus is $(35^{+8}_{-5})°$. The half-opening angle of the torus, $\theta^{\rm ir}_{\rm L} = (36^{+9}_{-6})°$, is indistinguishable from $\theta^{\rm ir}_{\rm V}$. The inner-to-outer radius ratio of the torus is $0.016^{+0.006}_{-0.004}$, while the ratio of the torus height to the outer radius is $0.16^{+0.06}_{-0.04}$. We compare these values to those previously reported in the literature (Hines & Wills 1993; Hines et al. 1999; Tran et al. 2000; Burtscher et al. 2013) in Sections 5.1 and 5.4.

The torus geometry assumed in the Efstathiou & Rowan-Robinson (1995) models means that the mid-IR emission is anisotropic, with viewing angles closer to edge-on tending to suppress the mid-IR emission (Efstathiou 2006; Efstathiou et al. 2014). The derived combination of torus geometry and viewing angle of IRAS 09104+4109 thus implies a (multiplicative) anisotropy correction to the AGN luminosity of $0.83^{+0.08}_{-0.07}$. The derived *intrinsic* AGN infrared luminosity is thus $\sim 4.9 \times 10^{46}$ erg s^{-1}, and the total IR luminosity (assuming that the starburst emission is isotropic) is $\sim 5.5 \times 10^{46}$ erg s^{-1}.
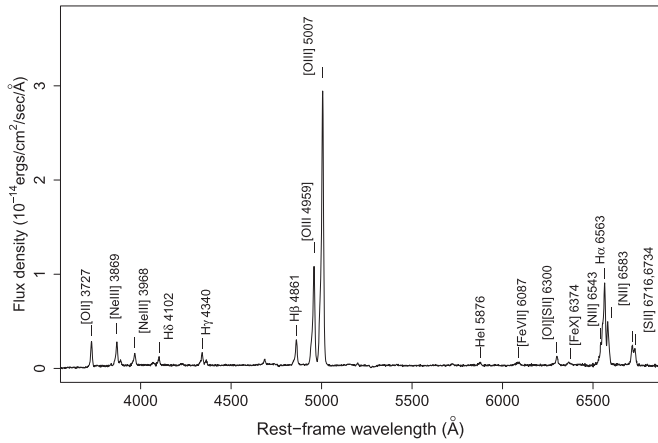
Figure 2. Optical spectrum of IRAS 09104+4109 taken with the Double Spectrograph at Palomar Observatory. Together with the canonical emission lines, there are weak but clear detections of two coronal iron lines. Line fluxes are given in Table 3.

The optical spectrum is shown in Figure 2. From it, we derive $z = 0.4416 \pm 0.0001$. The optical spectrum shows multiple narrow emission lines (Table 3; see also Tran et al. 2000). Analysis of the spectrum was conducted within IRAF. Lines were identified using line lists assembled from previous observations of starbursts and AGNs (Farrah et al. 2005; Shirazi & Brinchmann 2012). Line fluxes and EWs were measured by marking two continuum points, one on each side of the line, and fitting a linear continuum. The errors were found by estimating the variance in the continuum and remeasuring the EW using the variance as the continuum level.

Our spectrum is consistent within the errors with that of Tran et al. (2000); given that their spectrum is of higher quality than ours, we only comment on the lines in the additional wavelength coverage of our spectrum. We detect the canonical emission lines, including Hα, [N II], and [S II] lines. From our spectrum, IRAS 09104+4109 is unambiguously classified as a Seyfert using standard emission-line diagnostics (Baldwin et al. 1981) and lies well away from the regions proposed as harboring composite AGN/starburst systems (e.g., Kewley et al. 2001; Stasińska et al. 2006). In addition, we detect two high-excitation "coronal" iron lines: [Fe VII] $\lambda6087$ and [Fe X] $\lambda6375$, at 2.8σ and 2.9σ significance, respectively. These iron lines have been seen in ULIRGs (Farrah et al. 2005) but are more commonly observed in supernova remnants and in the solar corona (hence their name). They are rare in extragalactic objects (but see Osterbrock 1981; Reynolds et al. 1997; Gelbord et al. 2009; Rose et al. 2015, for examples). They are discussed further in Section 5.4.

4. X-RAY ANALYSIS

4.1. Overview

We use Xspec (Arnaud 1996) version 12.8.2 for spectral modeling of the *NuSTAR*, *Swift*, *Suzaku*, and *Chandra* data. To model the soft X-ray data, we follow results from previous studies and use two MEKAL plasma components (Mewe et al. 1985; Liedahl et al. 1995) with temperatures determined directly from the data. In the fits to the (joint) data we keep the temperatures the same for all instruments but allow normalizations to vary independently, because different instruments' point-spread functions (PSFs) sample the diffuse emission

Table 2
X-ray Observations of IRAS 09104+4109 Used in This Paper

Observatory and Instrument	Observation Start Date	Exposure (ks)	Source Count Rate (10^{-2} s^{-1})
NuSTAR/FPMA	2012 Dec 26	15.2	3.4 ± 0.2
Swift/XRT	2012 Dec 25	5.9	5.0 ± 0.3
Suzaku/XIS1	2011 Nov 18	81.3	12.6 ± 0.1
Chandra/ACIS	2009 Jan 06	69.3	1.09 ± 0.04

Note. Count rates are background-subtracted rates for one of the instruments of a given observatory, within the source extraction region and bandpass used for fitting (see Sections 2.2 and 4 for details).

Table 3
Emission-line Properties of IRAS 09104+4109 Measured from the Palomar Double Spectrograph

Line	Flux (10^{-14} erg cm^{-2} s^{-1})	Rest EW (Å)
[S II] $\lambda6734$	2.24 ± 0.15	58 ± 20
[S II] $\lambda6716$	2.63 ± 0.15	62 ± 15
[N II] $\lambda6583$	6.44 ± 0.62	141 ± 15
Hα $\lambda6563$	8.24 ± 0.44	183 ± 14
[N II] $\lambda6543$	3.47 ± 0.80	78 ± 11
[Fe X] $\lambda6374$	0.60 ± 0.20	17 ± 10
[O I]+[S III] $\lambda6300$	1.42 ± 0.30	40 ± 17
[Fe VII] $\lambda6087$	0.77 ± 0.27	23 ± 13
He I $\lambda5876$	0.48 ± 0.15	15 ± 8

Note. A higher-resolution, deeper optical spectrum is available in Tran et al. (2000). We here present those lines that are uniquely present in our spectrum due to our longer-wavelength coverage, plus two lines in the wavelength range in which our data overlap with Tran et al. (2000). See also Crawford & Vanderriest (1996) and Soifer et al. (1996).

differently, and spatial variation in temperature has previously been found (O'Sullivan et al. 2012). Other MEKAL parameters are kept fixed at the values determined in previous work: $n_H = 5$ cm^{-3} and $Z = 0.4\,Z_\odot$. Since much of the diffuse emission is subtracted from the small-scale *Chandra* spectrum, we set the normalization of one of the two MEKAL components to zero for these data and model the residual plasma contribution with the remaining MEKAL component. Due to the limited quality of the *Swift*/XRT spectrum, we also use only a single MEKAL component to model it. All models include Galactic absorption ($N_{H,G} = 1.4 \times 10^{20}$ cm^{-2}; Kalberla et al. 2005) and the same redshift, $z = 0.442$, for all components.

To model the hard X-ray data from *NuSTAR*, *Swift*, *Suzaku*, and *Chandra*, we use two model sets:

1. T+R—a phenomenological model consisting of two independent components, one transmitted (T) and one reflected (R). The T component is an absorbed power law modeled by Xspec model wabs × cabs × cutoffpl, which accounts for Compton scattering and has a fixed *e*-folding scale of 200 keV. The R component is modeled using pexrav (Magdziarz & Zdziarski 1995) and a narrow Gaussian emission line at 6.4 keV representing fluorescent iron Kα emission.

2. Torus models—observationally motivated geometric models, in which the T and R components are self-consistently calculated and coupled. We consider two

torus models, MYtorus (Murphy & Yaqoob 2009) and BNtorus (Brightman & Nandra 2011).

The T+R model has been used by many previous authors, so we employ it to allow for straightforward comparisons. It was predominantly used in one of two extremes, transmission-dominated (TD) and reflection-dominated (RD), where one of the components was assumed to be negligible. However, the key to insights into the properties of the X-ray obscurer is the ability to model both components (Yaqoob 2012), unless the obscuration is so high ($N_H \gtrsim 10^{25}\,\mathrm{cm}^{-2}$) that only the R component is observable (e.g., Arévalo et al. 2014; Baloković et al. 2014; Gandhi et al. 2014; Annuar et al. 2015; Bauer et al. 2015). Here we start with two components and let the data determine whether either component is negligible. This model does not have a physical geometry, but has nevertheless been used in the literature to account for spectral features attributed to the AGN torus. In particular, pexrav assumes a slab geometry rather than a torus, so the viewing angle changes the spectrum at the level of only a few percent over most of the $0°$–$90°$ range. The viewing angle is kept fixed ($\cos\theta_V = 0.45$) because it cannot be interpreted in the context of the torus, so it should not be compared to other viewing angles discussed in this paper. This model also includes an unresolved Gaussian line fixed at $E = 6.4\,\mathrm{keV}$ ($\sigma = 10^{-3}\,\mathrm{keV}$), accounting for fluorescent emission of iron arising from the same material producing the R component. We keep the elemental abundances in pexrav fixed at solar values and the normalization of the 6.4 keV line independent of the pexrav normalization.

In contrast, MYtorus and BNtorus are models for the obscurer with an observationally motivated geometry, that of a smooth toroidal obscurer. The geometry assumed in the MYtorus model is a torus with a fixed inner half-opening angle of $\theta_L^{my} = 60°$. The column density in the line of sight (N_H) is a function of viewing angle and varies from maximum for a viewing directly through the equator (where $N_H = N_{H,eq}$) to zero when the line of sight just grazes the torus edge. In the BNtorus model the torus is approximated as a sphere with symmetric conical cutouts and the inner half-opening angle θ_L^{bn} can be varied as a fitting parameter. The column density has a single value along any line of sight that intersects the torus; that is, as long as $\theta_V^{bn} > \theta_L^{bn}$, then the line-of-sight column density N_H is equal to the equatorial column density $N_{H,eq}$. Since the normalizations of different spectral components are internally linked due to the obscurer geometry, two degrees of freedom (ν) are removed from the fits with respect to the T+R model. In both torus models the Fe Kα line strengths are self-consistently calculated.

We describe the T+R model fits in Section 4.2 and the torus modeling in Section 4.3. The parameters of the X-ray models for the AGNs are summarized in Table 4. We consider models for the diffuse emission separately in Section 4.4.

4.2. The T+R Model

We first model only the simultaneous *Swift* and *NuSTAR* spectra, which are well matched in signal-to-noise ratio across the broad 0.5–50 keV bandpass. Fitting the T+R model, we find that the photon index, Γ, cannot be constrained. Any photon index in the range $1.4 < \Gamma < 2.6$ fits the data equally well as the canonical $\Gamma = 1.8$ (e.g., Dadina 2008; Rivers et al. 2013; Malizia et al. 2014). Fixing Γ at 1.8, the best fit ($\chi^2/\nu = 76.7/63$) is for a model with the intrinsic power-law

Table 4
Summary of Modeling of the X-ray Spectrum

Model Parameter	Data: *NuSTAR* with	
	Swift/XRT	*Suzaku* and *Chandra*
T+R Model		
χ^2/dof	76.7/63[a]	1268/1381
Γ	[1.6, 2.1]	$1.8^{+0.2}_{-0.4}$
$L_{2-10\,\mathrm{keV}}$	[4, 100]	0.8 ± 0.3
N_H	>4	$0.5^{+0.3}_{-0.2}$
MYtorus Model		
χ^2/dof	78.8/65	1299/1381
Γ	1.8 (f)	<1.8[b]
$L_{2-10\,\mathrm{keV}}$	9 ± 2	1.1 ± 0.1
$N_{H,eq}$	2^{+4}_{-1}	0.9 ± 0.2[c]
N_H	$=N_{H,eq}$	0.5 ± 0.1
θ_V^{my}	90 (f)	65 (f)
BNtorus Model[d]		
χ^2/dof	73.9/64	1276/1379
Γ	1.8 (f)	1.6 ± 0.2
$L_{2-10\,\mathrm{keV}}$	[8, 20]	[1.2, 1.8]
$N_{H,eq} = N_H$	>2	0.4 ± 0.1
θ_V^{bn}	$[\theta_L^{bn}, 90]$	$[\theta_L^{bn} + 5, \theta_L^{bn} + 15]$

Notes. Spectral parameters are intrinsic photon index (Γ), intrinsic 2–10 keV luminosity ($L_{2-10\,\mathrm{keV}}$, in units of $10^{45}\,\mathrm{erg\,s}^{-1}$), line-of-sight column density (N_H, in $10^{24}\,\mathrm{cm}^{-2}$), equatorial column density ($N_{H,eq}$, in $10^{24}\,\mathrm{cm}^{-2}$), viewing angle ($\theta_V$, in degree), and torus half-opening angle (θ_L, in degree). Numbers in square brackets denote ranges, and fixed parameters are followed by (f).
[a] Evaluated for $\Gamma = 1.8$ and $N_H = 4$ (in the same units); $\Delta\chi^2 < 1$ for the parameters' ranges shown here.
[b] Best fit is $\Gamma = 1.6$, which is the edge of the parameter domain for Γ.
[c] For $\Gamma = 1.8$, $N_{H,eq} = 1.1^{+0.2}_{-0.1}$ (in the same units).
[d] Since angles θ_V^{bn} and θ_L^{bn} cannot be constrained independently, we express constraints on θ_V^{bn} in terms of θ_L^{bn}.

continuum absorbed by $N_H \sim 4 \times 10^{24}\,\mathrm{cm}^{-2}$, with contributions from both T and R components. However, valid solutions exist with no absorbed component present. In the best-fit solution, the T component dominates at energies above 20 keV. Assuming a harder photon index ($\Gamma \approx 1.6$) leads to TD solutions, while a softer assumed index ($\Gamma \approx 2.1$) gives RD solutions. In either case, χ^2 increases by less than 1 with respect to the best fit. The diverse range of models consistent with this data set constrains the intrinsic 2–10 keV luminosity to lie between $4 \times 10^{45}\,\mathrm{erg\,s}^{-1}$ and $1 \times 10^{47}\,\mathrm{erg\,s}^{-1}$.

To provide more stringent constraints on the models, we model the *NuSTAR* data (taken in 2012 December) together with archival *Suzaku* and *Chandra* data (taken in 2011 November and 2009 January, respectively). The *Swift*, *Suzaku*, and *Chandra* data are consistent with each other, but because of poorer photon statistics, we exclude the *Swift* data from modeling. With the additional *Suzaku* and *Chandra* data, the constraints on the photon index and the absorption column improve significantly. Note that in this case, the very high signal-to-noise ratio of the soft X-ray data constrains models better than the *NuSTAR* data in the overlapping energy range.

We find the best fit ($\chi^2/\nu = 1268/1381$) for $\Gamma = 1.8^{+0.2}_{-0.4}$ and $N_H = (5^{+3}_{-2}) \times 10^{23}\,\mathrm{cm}^{-2}$. This model is shown in Figure 3. The soft X-ray data alone drive the fit toward hard photon
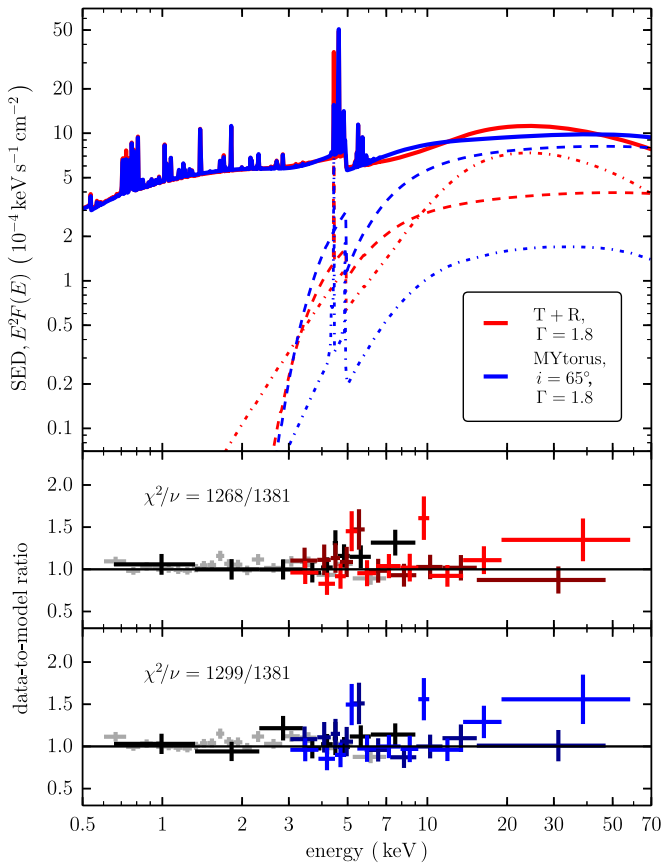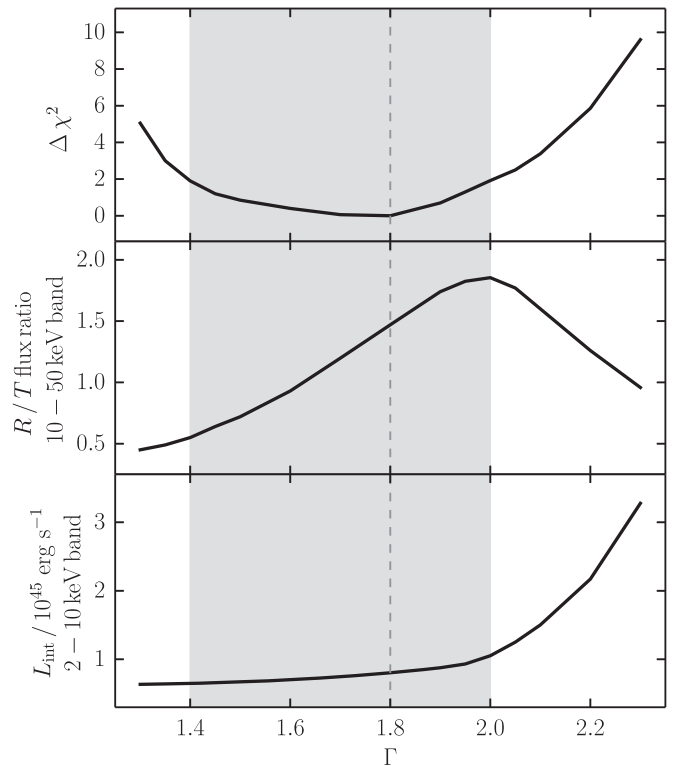
Figure 3. Comparison of best-fit models for the *NuSTAR*, *Suzaku*, and *Chandra* data. A phenomenological T+R model is shown by the red lines, while blue lines show a `MYtorus` model. Solid lines are for the total spectrum (AGN and diffuse emission), dashed lines are for the transmission components, and dot-dashed lines are for the reflection components. Plasma components making up the diffuse emission are not plotted in order to avoid confusion; any flux not contributed by the AGN components is due to plasma emission. The lower panels show the data-to-model ratio for each of the two models. Colored lines are for the *NuSTAR* data (darker color for FPMA, brighter color for FPMB), gray is for *Suzaku*, and black is for *Chandra*.

Figure 4. Phenomenological description of the AGN spectrum of IRAS 09104 +4109 as a function of the intrinsic photon index. For $\Gamma \approx 1.4$ the 10–50 keV band is dominated by the T component, while for $\Gamma \approx 2.0$ the R component dominates, as shown in the middle panel. The joint *NuSTAR*, *Suzaku*, and *Chandra* data constrain the photon index to $\Gamma = 1.8^{+0.2}_{-0.4}$, marked with the gray shaded area and the vertical dashed line. Within this confidence interval, the intrinsic 2–10 keV luminosity is well constrained, as shown in the bottom panel. For comparison, the fits based only on the simultaneous *NuSTAR* and *Swift*/XRT data transition from being dominated by the T component to being dominated by the R component within a narrower range of $1.7 < \Gamma < 2.0$. In that case, the intrinsic luminosity spans more than an order of magnitude within the range of Γ plotted here, while the change in χ^2 barely exceeds unity over that parameter range.

indices ($\Gamma < 1.5$) and a TD model (Chiang et al. 2013). The addition of *NuSTAR* data constrains Γ to a more typical value and results in a solution where T and R components contribute to the hard X-ray flux nearly equally. Figure 4 illustrates how the χ^2, the relative contributions of T and R components, and the implied intrinsic luminosity vary within the 90% confidence interval for the photon index (1.4–2.0). The intrinsic 2–10 keV luminosity of the best-fit model is $(8 \pm 3) \times 10^{44}$ erg s^{-1}.

Additional constraints can be drawn from the equivalent width (EW) of the neutral Fe Kα line.[29] The low EW of this line (EW $\simeq$ 0.3 keV) in the *NuSTAR*, *Swift*, and archival data argues against an RD scenario, since RD spectra usually have Fe Kα EWs of ~1 keV. On the other hand, a weak iron line could also arise if the iron abundance is ~30% solar, which is plausible given that subsolar abundance has been inferred for the diffuse plasma (e.g., O'Sullivan et al. 2012). Constraints based on the Fe Kα line are discussed in Chiang et al. (2013); due to the inferior spectral resolution of *NuSTAR* compared to

Chandra around 6.4 keV ($\simeq$0.4 keV compared to $\simeq$0.13 keV), the new data do not alter their conclusions.

4.3. The Torus Models

We start by applying the `MYtorus` model to the simultaneous *Swift* and *NuSTAR* data. Due to limited photon statistics, we can only draw tentative conclusions. If we fix Γ to 1.8 and assume that the torus is viewed edge-on ($\theta_V^{my} = 90°$), then a good fit ($\chi^2/\nu = 78.8/65$) is found for $N_H = (2^{+4}_{-1}) \times 10^{24}$ cm^{-2}. In this case the equatorial column density of the torus, $N_{H,eq}$, equals the column density observed along the line of sight to the nuclear X-ray source, N_H. If we let viewing angle vary, then this implies lower N_H, but for $\theta_V^{my} < 75°$ the fits only produce a lower limit on $N_{H,eq}$ of about 3×10^{24} cm^{-2}. There is perhaps a slight preference for viewing angles closer to $\theta_V^{my} = 60°$ (i.e., the edge of the torus in the `MYtorus` model), but the corresponding change in χ^2, relative to edge-on inclination, is less than 2. The solutions are generally RD, with EWs of Fe Kα of $\leqslant$1.2 keV. The implied intrinsic luminosity in the 2–10 keV band is $(9 \pm 2) \times 10^{45}$ erg s^{-1}.

Applying the `MYtorus` model to the joint *NuSTAR*, *Suzaku*, and *Chandra* data set, we find a preference away from edge-on

---

[29] We evaluate the EW of the Fe Kα line by taking the ratio of line flux to flux density of the AGN continuum components only, i.e., excluding the plasma components that otherwise dominate up to the Fe Kα line energy at 6.4 keV, except for the small-scale *Chandra* spectrum. We use a band spanning rest frame 5.7–6.7 keV.

inclination. Due to the geometry assumed in the model, viewing angles within $\sim5°$ of $60°$ (where the line of sight skims the torus) require caution, as N_H changes steeply with viewing angle—this can lead to unreasonably tight constraints on some model parameters. We therefore fix θ_V^{my} to $65°$. The best fit is an effectively TD model, with the R component contributing $\lesssim20\%$ to the 10–50 keV band and an Fe Kα EW of 0.3 ± 0.1 keV. This is consistent with the low Fe Kα EW found with the same data using the T+R model. The equatorial column density of the torus, $N_{H,eq}$, is $(9 \pm 2) \times 10^{23}$ cm^{-2} for Γ in the range of 1.6–1.8. The best-fit photon index is 1.6, but this is at the lower end of the parameter domain for the MYtorus model, so a true lower limit to the confidence interval cannot be determined. Assuming a statistically acceptable value of $\Gamma = 1.8$ leads to $N_{H,eq} = (1.1^{+0.2}_{-0.1}) \times 10^{24}$ cm^{-2}. The intrinsic 2–10 keV luminosity from this model is $(1.1 \pm 0.1) \times 10^{45}$ erg s^{-1}. This fit is shown in Figure 3.

Applying the BNtorus model to the *Swift* and *NuSTAR* data, we find an equally good fit as the MYtorus model. Assuming $\Gamma = 1.8$, the best fit ($\chi^2/\nu = 73.9/64$) is found for $N_H > 2 \times 10^{24}$ cm^{-2}. Again, this is an RD solution, with the N_H constrained from the upper side only by the parameter domain limit ($<10^{26}$ cm^{-2}). We find that θ_V^{bn} and θ_L^{bn} cannot be constrained by the data simultaneously; however, fixing θ_L^{bn} always leads to θ_V^{bn} lying between $\gtrsim(\theta_L^{bn})°$ and edge-on. The implied 2–10 keV intrinsic luminosity lies between 8×10^{45} erg s^{-1} and 2×10^{46} erg s^{-1}.

The BNtorus model applied to the joint *NuSTAR*, *Suzaku*, and *Chandra* data does not provide simultaneous constraints on θ_V^{bn} and θ_L^{bn} either. They are constrained in the sense that their difference is $\gtrsim5°$ for any one assumed angle within their respective parameter ranges, $18°$–$87°$ for θ_V^{bn} and $26°$–$84°$ for θ_L^{bn}, which is consistent with the Sy2 classification (i.e., that the *optical* Broad Line Region (BLR) is not seen in direct light). We find best fits ($\chi^2/\nu = 1276/1379$) consistent with $\Gamma = 1.6 \pm 0.2$ and $N_H = (4 \pm 1) \times 10^{23}$ cm^{-2} for a broad range of viewing angles. Intrinsic 2–10 keV luminosities for these solutions are in the range $(1.2–1.8) \times 10^{45}$ erg s^{-1}. Although the T and R components, as well as iron lines, cannot be separated in this model, equivalent phenomenological solutions reveal that the T component dominates the >10 keV flux. The best-fit solution is therefore qualitatively similar to that obtained from the MYtorus model.

4.4. Diffuse Emission Models and Multi-epoch Flux Comparison

In the modeling presented in Sections 4.2 and 4.3, the diffuse emission was included, but the focus was on the AGN emission. It is, however, worth briefly discussing the diffuse emission models, for two reasons. First, while the literature is consistent in modeling the extended emission, details and best-fit parameters differ between studies. Second, with relatively high temperatures, the diffuse plasma emission significantly contributes to the emission into the *NuSTAR* band, up to $\simeq10$ keV.

As the extended emission exhibits significant spatial variations in plasma temperature (O'Sullivan et al. 2012), a cross-instrument comparison based on a simple one- or two-component MEKAL model is only approximate. However, we did not find it necessary to add complexity to the model based on fitting statistics or structured residuals. We find best-fit

plasma temperatures in the range of 1–4 keV and 5–8 keV, based mostly on *NuSTAR* and *Suzaku* data. For any single model fit (recalling that we only use a single MEKAL model for both the *Chandra* and *Swift*/XRT data; see Section 4.1), the typical 90% uncertainty on the temperature is 0.4–1.5 keV when *NuSTAR* is combined with the archival data, and approximately 2 keV when combined with *Swift*/XRT. These results are similar to all previous studies.

The most direct comparison can be made between *NuSTAR* and *Chandra* spectra extracted from the same $50''$ circular region. In this case we find that the total flux in the 3–8 keV band is $(1.0 \pm 0.1) \times 10^{-12}$ erg s^{-1} cm^{-2} in both instruments. Assuming that the *Swift*/XRT extraction contains most of the diffuse emission, its 3–8 keV flux of 9.3×10^{-13} erg s^{-1} cm^{-2} is also consistent with *NuSTAR* within the typical spread found in other simultaneous observations. The cross-normalization between the two modules of *NuSTAR*, as well as those of *Suzaku*, is within 5% of unity in all models. We thus find that no significant spectral variability occured between *Chandra*, *Suzaku*, *NuSTAR*, and *Swift* observations, and that all cross-normalizations discussed here are well within their respective expectations (Madsen et al. 2015).

The extended soft X-ray emission spans several tens of kiloparsecs (O'Sullivan et al. 2012) and therefore should not vary on a timescale spanning the observations used here. We confirm this based on spectra extracted from large circular regions ($100''$ for *Suzaku* and *Chandra*). The small-scale *Chandra* spectrum (within $1''$) is dominated by AGN emission above 3 keV according to nearly all models, with a flux in the 3–8 keV band of $(4.0 \pm 0.2) \times 10^{-13}$ erg s^{-1} cm^{-2}. In the *NuSTAR* spectra, the diffuse emission contributes approximately 10% of the flux even at 10 keV.

The 3–8 keV flux from the best-fit AGN components in different models ranges from 3.6×10^{-13} erg s^{-1} cm^{-2} to 3.9×10^{-13} erg s^{-1} cm^{-2}, which is consistent with the nuclear *Chandra* flux. With our 2–10 keV flux of $(1.2–3.6) \times 10^{-13}$ erg s^{-1} cm^{-2} (AGN components alone, based on the *NuSTAR* data), we find excellent agreement with the flux estimated by Chiang et al. (2013) assuming two different AGN models based on *Chandra* and *Suzaku* data, ranging over $(1.8–3.3) \times 10^{-13}$ erg s^{-1} cm^{-2}. The *XMM-Newton*-based estimate of Piconcelli et al. (2007), $(4.7–5.5) \times 10^{-13}$ erg s^{-1} cm^{-2}, is in apparent disagreement with ours, although their prediction for hard X-ray flux (20–30 keV) matches the *NuSTAR*-detected flux well. A discrepancy of this magnitude may be due to the PSF of *XMM-Newton* sampling the diffuse emission differently, resulting in different best-fit models; however, variability of the AGN cannot be excluded.

AGN variability is also suggested by the hard X-ray data, where contamination by the diffuse emission is negligible. Both the *NuSTAR* detection and the *Suzaku*/PIN upper limit put the 20–100 keV flux ($\simeq3 \times 10^{-12}$ erg s^{-1} cm^{-2} and $<6 \times 10^{-12}$ erg s^{-1} cm^{-2}) below the *BeppoSAX* detection (Franceschini et al. 2000) at $\simeq1 \times 10^{-11}$ erg s^{-1} cm^{-2}. The *BeppoSAX* flux in the 20–30 keV band, $2.6^{+1.9}_{-1.6} \times 10^{-12}$ erg s^{-1} cm^{-2} (Piconcelli et al. 2007), exceeds the *Swift*/BAT detection limit of $\simeq1.5 \times 10^{-12}$ erg s^{-1} cm^{-2} (Vignali et al. 2011), as well as most extrapolations from later soft X-ray studies (e.g., $(7–15) \times 10^{-13}$ erg s^{-1} cm^{-2} by Chiang et al. 2013; $(6–13) \times 10^{-13}$ erg s^{-1} cm^{-2} by Piconcelli et al. 2007) and the *NuSTAR*-detected flux of $\simeq7 \times 10^{-13}$ erg s^{-1} cm^{-2}. While it is possible that the high

BeppoSAX flux was due to contamination by a nearby hard X-ray source (Piconcelli et al. 2007; Vignali et al. 2011; Chiang et al. 2013), the possibility of variability in luminosity and/or line-of-sight column density is naturally explained in our models, where the transmitted (T) component dominates the AGN spectrum.

5. DISCUSSION

The IR, optical, and X-ray data together form a consistent picture of the central engine in IRAS 09104+4109. Starting with the IR data, we build this picture in Section 5.1 through Section 5.4.

5.1. The Infrared Data

Our results are consistent with previous studies that mark IRAS 09104+4109 as AGN dominated (Rowan-Robinson 2000; Sargsyan et al. 2008; Rowan-Robinson & Wang 2010; Ruiz et al. 2013). By modeling the IRS spectrum together with longer-wavelength data up to 1000 μm, we draw several new constraints. We clearly detect ongoing star formation in IRAS 09104+4109 (see also Han & Han 2012). The star formation rate, at $110^{+35}_{-28} M_\odot$ yr^{-1}, is consistent with rates seen in $z < 0.2$ ULIRGs (Farrah et al. 2003) and suggests that IRAS 09104+4109 is going through a significant episode of star formation despite the dominance of the AGN in the IR. The excellence of the fit is consistent with our initial assumption that there is only one current episode of star formation in IRAS 09104+4109. Compared to the rate derived from optical observations (Bildfell et al. 2008), it implies that optical data underestimate the star formation rate in IRAS 09104+4109 by approximately a factor of three.

The 3σ upper limit on the age of the starburst of 50 Myr is inconsistent with the range of 70–200 Myr derived by Pipino et al. (2009). Moreover, the fit to the IR SED does not require a contribution from a second, older starburst. It is unlikely that this inconsistency arises due to model degeneracies in the IR SED fitting, since we consider all possible solutions when deducing the starburst age constraint. Instead, this implies that only the star formation seen by Bildfell et al. (2008) contributes to the IR emission, with no contribution from the event inferred by Pipino et al. (2009). Furthermore, since the radio jets have an age of 100–160 Myr (O'Sullivan et al. 2012), it is unlikely that the ongoing star formation was triggered by the jets, or by the event that triggered the jets. This suggests that IRAS 09104+4109 is currently going through a *second* major epoch of luminous activity in the past 200 Myr. This is consistent with the relatively small amount of molecular gas in this system (Evans et al. 1998; Combes et al. 2011) and suggests that IRAS 09104+4109 will soon become a quiescent galaxy. The upper limit on the starburst age is also consistent with the absence of Ca absorption in the optical spectrum, which suggests a relative dearth of A-type stars.

We cannot, however, set useful constraints on the spatial scale of the starburst. At $z = 0.442$, 1″ corresponds to 5.7 kpc. Compared to the spatial resolution of the IRS (3″7 and 10″5 for the two low-resolution modules) and 5–10″ for PACS, this gives a spatial resolution of 21–39 kpc. We thus cannot say whether the star formation is nuclear, spread throughout the host, or some combination of the two.

Our study is the first to set IR-based constraints on the geometry of the AGN obscurer; assuming the that geometry in the Efstathiou & Rowan-Robinson (1995) models holds, we derive $\theta_V^{ir} = 35^{+8}_{-5}{}^\circ$ and $\theta_L^{ir} = 36^{+9}_{-6}{}^\circ$. These values are consistent with the requirement, from the Sy2 classification, that no broad lines are visible in direct light, i.e., that $\theta_V^{ir} > \theta_L^{ir}$. Constraints on the geometry of the optical obscurer have been set, though these constraints depend on the degree of polarization and the assumed model (e.g., Brown & McLean 1977); Hines et al. (1999) obtain $\theta_V^o = 34$–41° and $\theta_L^o = 15$–33°, while Tran et al. (2000), who find a higher polarization, argue for $\theta_V^o \simeq 50°$ and $\theta_L^o \simeq 40°$ (see also Hines & Wills 1993). Assuming that the IR and optical obscurers are coaligned and that $\theta_V^o = \theta_V^{ir}$, our values are more consistent with those of Hines et al. (1999). We find, however, that $\theta_V^{ir} \simeq \theta_L^{ir}$, whereas both Hines et al. (1999) and Tran et al. (2000) argue that θ_L^{ir} is less than θ_V^{ir}, by 14° and 10°, respectively. Such a difference is not entirely inconsistent with the IR-derived values, but it is also plausible that the optical obscurer has a smaller half-opening angle than the IR obscurer.

5.2. The X-Ray Data

We start by summarizing the X-ray analysis presented in Section 4. Our X-ray modeling can be separated into two branches: the simultaneous *Swift*/XRT and *NuSTAR* data, which feature a constant and relatively low signal-to-noise ratio across the 0.5–50 keV energy range, versus the joint *NuSTAR* and archival *Chandra* and *Suzaku* data, among which differences in constraining power are large and complex, and the *NuSTAR* contribution is smaller. The latter data set prefers Compton-thin TD models with $N_H \sim 5 \times 10^{23}$ cm^{-2}, including a tilted torus solution in which $N_{H,eq}$ exceeds the Compton-thick threshold. The *Swift*/XRT and *NuSTAR* data lead to Compton-thick RD solutions for the AGN with each of the models, implying significantly higher intrinsic luminosity. Despite the possible issue of nonsimultaneity, we consider the joint *NuSTAR*, *Chandra*, and *Suzaku* data set to be more reliable and therefore base our further discussion only on the results it provides.

We started with the T+R models; the *NuSTAR* detection disfavors the scenario where a hard, luminous, and strongly absorbed T component dominates the flux above 10 keV. The preference for softer photon indices rules out the hard values ($\Gamma < 1.5$) discussed in, e.g., Piconcelli et al. (2007) and Chiang et al. (2013). Dominance of the R component in the hard X-ray band is not favored either, as the EW of Fe Kα is relatively low. Instead, IRAS 09104+4109 resembles heavily obscured AGNs in the nearby universe, in which both T and R components contribute to the X-ray spectrum in the *NuSTAR* band (e.g., Puccetti et al. 2014; Koss et al. 2015; M. Baloković et al. 2016, in preparation). In terms of both spectral components and data quality, the constraints are similar to the type 2 quasars Mrk 34 (Gandhi et al. 2014) and SDSS J1218+4706 (Lansbury et al. 2015), although both of those objects likely have higher line-of-sight column densities than IRAS 09104+4109. The shapes and relative contributions of the T and R components depend on the geometry of the obscurer; however, the T+R model is only approximate, and more appropriate torus models are needed in order to derive physical constraints.

Turning to the torus models, modulo the difference in the assumed geometry and the dependence of N_H on the viewing angle, the parameters inferred from fitting the `MYtorus` and `BNtorus` models to the combined X-ray data set are

indistinguishable. Both are consistent with scenarios where the line of sight skims the edge of the torus, thus giving rise to an Sy2 classification only by a few degrees. Moreover, both imply intrinsic luminosities in the 2–10 keV band in the range of $(1–2) \times 10^{45}$ erg s^{-1}. Notably though, the *NuSTAR* data are not decisive. With the *NuSTAR* data there is less of a χ^2 gradient toward hard photon indices. However, with the assumptions used in this analysis, the same solutions can be found from the archival data alone, albeit with larger uncertainties. Relaxing the assumed spectral parameters of the plasma model for the soft X-ray part of the spectrum creates severe degeneracies such that the model becomes RD for hard Γ, i.e., opposite of the behavior described in Section 4.2. Although fluxes in overlapping spectral bands between *NuSTAR*, *Swift*, *Suzaku*, and *Chandra* are consistent (see Section 4.4), spectral variability between the observations and the resulting biases in joint fitting cannot be fully excluded. Despite its coverage above 10 keV, the current *NuSTAR* data are insufficient to uniquely constrain the AGN spectrum, so the fits remain susceptible to the assumptions in modeling the soft X-ray data.

5.3. The X-Ray and Infrared Data

We now consider the X-ray and IR AGN torus models together. A cautionary note is warranted: the models for the X-ray include gas but not dust, while the models for the IR emission include only dust. In considering the two together we are thus comparing different structures.

We first compare the derived X-ray and IR luminosities. Gandhi et al. (2009) have derived a relationship between 2–10 keV luminosity and 12.3 μm luminosity density for Seyferts, albeit using a sample more than two orders of magnitude less luminous than IRAS 09104+4109, on average. Taking the 12.3 μm AGN luminosity density from Figure 1 and translating it to a predicted 2–10 keV luminosity using the Gandhi et al. (2009) relationship yields $\sim 6.3 \times 10^{45}$ erg s^{-1}, a factor of ~ 3 higher than the 2–10 keV luminosity obtained from the torus models. Gandhi et al. (2009) also see that the type 2 quasars in their sample have a lower X-ray luminosity than is predicted by their relation, and argue that the reason for this is nuclear star formation that contaminates the 12.3 μm luminosity density. This, however, is an unlikely explanation for why IRAS 09104+4109 deviates from the relation, since the star formation in IRAS 09104+4109 is an order of magnitude less luminous than the AGN (the predicted 12.3 μm luminosity density of the starburst is even less than that of the AGN, but luminosities at specific wavelengths are less robust than total IR luminosities, so we are hesitant to make this comparison). This suggests that the proportionality between intrinsic X-ray and mid-IR (e.g., $\simeq 12$ μm) luminosities for AGNs may flatten at high luminosities (e.g., Stern 2015; but see also Asmus et al. 2015), or that a different relation is at work.

Turning to a comparison of the X-ray and IR geometries, it is reasonable to expect that the AGN structures producing the IR and the X-ray spectra are coaligned, which would make their respective viewing angles similar. Moreover, it is reasonable to expect their half-opening angles to be similar, motivated by comparisons of opening angles determined independently from X-ray and IR data (Brightman et al. 2015, Baloković et al. 2016). While the high X-ray luminosity of IRAS 09104+4109 would make it an excellent test for the trend of decreasing torus covering factor with

increasing X-ray luminosity observed for Compton-thick AGNs by Brightman et al. (2015), our modeling indicates that its line-of-sight obscuration is not significantly above the Compton-thick threshold, nor is the torus viewed close to edge-on. In this case, an independent constraint on the opening angle from the X-ray data would require a longer *NuSTAR* observation than the 15 ks presented here. For example, an exposure of 100 ks would provide $\simeq 10$ energy bins over the 10–50 keV band with signal-to-noise ratio better than 3, sufficient to constrain the photon index within 0.1 and the torus opening angle within approximately 20° (quoting 90% confidence intervals).

Coalignment of the IR and X-ray tori is consistent with the MYtorus and BNtorus results. In the MYtorus model, the half-opening angle, θ_L^{my}, is fixed to 60°, which is (just) within the 3σ range of the IR-derived torus half-opening angle. Using MYtorus, we find that viewing angles close to 60° fit the joint X-ray data set slightly better than edge-on ones. This is again just consistent with the result from the IR-based torus models. A useful constraint on the viewing angle can, however, be obtained only if the equatorial column density of the torus is assumed. For a borderline Compton-thick torus ($N_{H,eq} = 1 \times 10^{24}$ cm^{-2}) and the best-fit photon index ($\Gamma = 1.6$), $\theta_V^{my} = (65 \pm 2)°$. If, however, we use $\Gamma = 1.8$, then $\theta_V^{my} = (68^{+4}_{-2})°$. The difference in χ^2 for these two cases is negligible. This value of θ_V^{my} is still consistent with the Sy2 classification and (within the joint error budget) with the IR-derived value, but shows that with the current data MYtorus constrains the geometry of the X-ray obscurer only weakly.

The BNtorus constraints are stronger. Both θ_L^{bn} and θ_V^{bn} can be varied, but they cannot be independently constrained with the X-ray data. With reasonable assumptions, however, they are both consistent with the IR-based modeling results. If we fix θ_L^{bn} to 39°, as obtained from the IR modeling, then the best fit is found for $\theta_V^{bn} = (48^{+3}_{-2})°$. This combination of θ_L^{bn} and θ_V^{bn} is within 1σ of the IR-based geometry and represents a broad minimum in χ^2 (1274, for $\nu = 1379$) over the allowed range for those angles. In this case, we find $\Gamma = 1.7^{+0.1}_{-0.2}$ and $N_H = N_{H,eq} = (4.6^{+0.7}_{-0.9}) \times 10^{23}$ cm^{-2}.

Finally, the inferred bolometric luminosity from the X-ray models is consistent with that inferred from the IR models. Assuming an X-ray-to-bolometric correction of 50–130 (Marconi et al. 2004; Vasudevan & Fabian 2007; Lusso et al. 2012) leads to an estimate of $L_{bol} \sim (0.5–2.5) \times 10^{47}$ erg s^{-1}, based on the X-ray modeling alone. Instead starting from the anisotropy-corrected IR AGN luminosity and assuming that 30% of the bolometric emission emerges in the IR (Risaliti & Elvis 2004) yields $\sim 1.8 \times 10^{47}$ erg s^{-1}. Disregarding the anisotropy correction gives a still-consistent value of $\sim 2.3 \times 10^{47}$ erg s^{-1}.

5.4. The X-Ray, Infrared, and Optical Data

Finally, we fold in constraints from the optical data. The high-excitation iron lines in Figure 2 have three possible origins: a "coronal line region" (CLR) intermediate in distance between the broad- and narrow-line regions, the inner wall of a dusty torus, and the ISM several kiloparsecs from a "naked" Seyfert nucleus (Penston et al. 1984; Korista & Ferland 1989; Murayama & Taniguchi 1998). The third of these possibilities predicts that [Ne V] $\lambda 3426$ will be ~ 12 times stronger than [Fe X] $\lambda 6375$. This criterion is, at face value, consistent with
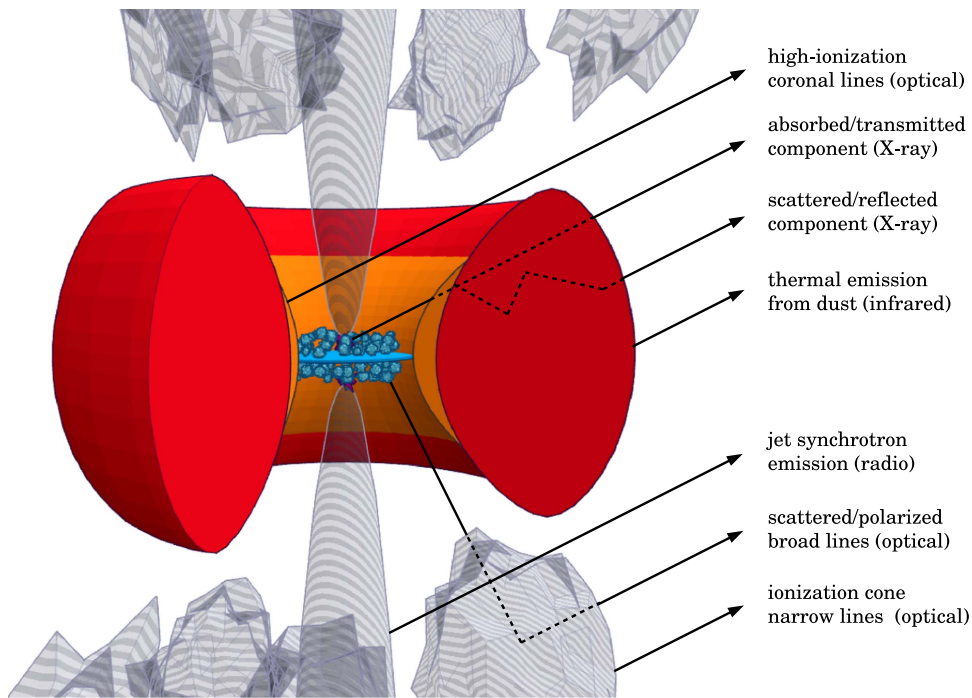
Figure 5. Sketch of the IRAS 09104+4109 nucleus geometry that is consistent with the IR, optical, and X-ray data (Section 5.4). The observer is in the direction of the black arrows. The bulk of the torus is shown in red, and its inner wall in orange. IR emission is due to warm dust in the torus, while the coronal lines in the optical spectrum come from the inner wall of the torus. X-rays pass through the torus; we distinguish contributions from the absorbed line-of-sight component (transmission; T) and from the component due to scattering (reflection; R). The accretion disk and the broad-line clouds are shown in blue, and the jet and narrow-line clouds in the ionization cone are shown in gray. The broad-line region is shielded from direct view by the vertical extent of the torus, but scattering in the ionization cones makes broad lines observable in polarized light. The ionization cones also emit narrow forbidden lines (most notably, O III), and the jet is observable at radio wavelengths.

our spectrum. If, however, we consider that [Fe X] $\lambda6375$ is almost certainly contaminated by [O I] $\lambda6364$, and take this contamination into account by assuming [O I] $\lambda6364$/[O I] $\lambda6300 = \frac{1}{3}$, then the [Ne V] $\lambda3426$/[Fe X] $\lambda6375$ ratio in IRAS 09104+4109 rises to ~40. Moreover, the IR-luminous nature of IRAS 09104+4109 argues that an origin in a CLR and/or in a dusty torus is more plausible.

The detection of [Fe X] $\lambda6375$ but not [Fe XIV] $\lambda5303$, if not due to differential obscuration between 5300 and 6400 Å, implies a range in hydrogen density along the line of sight of $3.0 < \log n_H (\mathrm{cm}^{-3}) < 5.8$ and a line of sight to a distance from the central ionizing source of 0.2–20 pc (Ferguson et al. 1997). We also note that the absence of both a 4000 Å break and stellar absorption features is consistent with a large population of young stars.

Combining the constraints from the IR, optical, and X-ray data is fraught with issues since the assumptions in the models were made without regard to each other. Moreover, the coronal iron lines are detected at just under 3σ significance in our spectrum. Nevertheless, the inference from the coronal iron lines of "just" seeing the inner wall of the torus is consistent with a line of sight that skims the torus—the CLR is visible in direct light, but the BLR can only be seen in scattered light (Tran et al. 2000). Moreover, the viewing angles inferred from the IR, optical, and X-ray data are consistent. Assuming that the geometry of the Efstathiou & Rowan-Robinson (1995) models is correct, this places the bulk of the dust column that composes the IR-emitting torus to within a vertical height of $z = 20$ pc of the nucleus. The X-ray obscurer is thus plausibly within this distance, also. The outer "edge" of the torus is then within 125 pc of the nucleus, and the inner edge is within 2 pc (see also Taniguchi et al. 1997). A sketch of this geometry is

shown in Figure 5. We do not draw detailed comparisons with literature values for AGN geometries due to the aforementioned issues with combining the data sets, but it is notable that the inner edge constraint is comparable to, though perhaps slightly larger than, that seen in AGNs with similar luminosities in Burtscher et al. (2013).

6. CONCLUSIONS

We have conducted a study of IRAS 09104+4109, an obscured hyperluminous quasar at $z = 0.442$, using X-ray data from *NuSTAR*, *Swift*, *Suzaku*, and *Chandra*, infrared data from *Spitzer* and *Herschel*, and an optical spectrum from Palomar. We apply radiative transfer models to the infrared data to measure rates of ongoing star formation in the host galaxy and to constrain the properties of the infrared obscurer around the AGN. We apply two types of models to the X-ray data—a T+R (phenomenological) model and the `MYtorus`/`BNtorus` (geometrical) models—to constrain the properties of the X-ray obscurer. We then fold in a distance constraint from the optical spectrum to construct a picture of the geometry of the structure around the AGN in this archetype object. Our conclusions are as follows:

1. The infrared data can be reproduced by a combination of an AGN and a starburst. The total infrared (rest-frame 1–1000 μm) luminosity is $(6.76 \pm 0.20) \times 10^{46}$ erg s^{-1}, with a contribution from the AGN of $5.94^{+0.26}_{-0.27} \times 10^{46}$ erg s^{-1}. The starburst is required in the fit at 3.7σ confidence, with a luminosity of $(5.54 \pm 1.48) \times 10^{45}$ erg s^{-1}, corresponding to a star formation rate of $(110^{+35}_{-28}) M_\odot$ yr^{-1}. Accounting for the anisotropic emission in the AGN models leads to an intrinsic AGN infrared luminosity of $\sim 4.9 \times 10^{46}$ erg s^{-1} and a total

infrared luminosity (assuming that the starburst emission is isotropic) of $\sim 5.5 \times 10^{46}$ erg s^{-1}. The ratio between the mid-infrared and 2–10 keV luminosities may deviate from that seen in lower-luminosity Seyferts, consistent with an intrinsically different relation at very high luminosities.

2. The infrared AGN torus model has a viewing angle (from pole-on) of $\theta_V^{ir} = (35_{-5}^{+8})°$ and a half-opening angle of $\theta_L^{ir} = (36_{-6}^{+9})°$. The starburst model is consistent with an age for the starburst of <50 Myr. The AGN model parameters are consistent with the requirement, from the Sy2 classification, that no broad lines are visible in direct light, i.e., that $\theta_V^{ir} > \theta_L^{ir}$. They are also consistent with the geometry of the (assumed) biconical structure giving rise to the optical emission lines. The star formation rate is comparable to those seen in lower-redshift ULIRGs and suggests that the host of IRAS 09104+4109 is going through a significant stellar mass assembly event. The age constraint is, however, inconsistent with both the age of the radio jets (120–160 Myr) and the age of a previous starburst event (70–200 Myr). This suggests that IRAS 09104+4109 underwent at least two epochs of luminous activity in the past ~ 200 Myr: one approximately 150 Myr ago, and one ongoing.

3. The X-ray model fits are consistent with $\Gamma \simeq 1.8$ and $N_H \sim 5 \times 10^{23}$ cm^{-2} (T+R: $\Gamma = 1.8_{-0.4}^{+0.2}$ and $N_H = (5_{-2}^{+3}) \times 10^{23}$ cm^{-2}; torus models: $\Gamma = 1.7_{-0.2}^{+0.1}$ and $N_H = N_{H,eq} = (4.6_{-0.9}^{+0.7}) \times 10^{23}$ cm^{-2}). The soft X-ray data alone drive the fit toward hard photon indices ($\Gamma < 1.5$) and a TD solution, but the addition of *NuSTAR* data results in a solution where T and R components contribute at comparable levels, and rules out an RD scenario in which line-of-sight obscuration and intrinsic luminosity would be much higher.

4. The constraints on the AGN obscurer geometry from the X-ray data are, with reasonable assumptions, consistent with those inferred from the infrared data. Fixing θ_L^{bn} to 39° in the `BNtorus` model gives a best-fit viewing angle of $\theta_V^{bn} = (48_{-2}^{+3})°$. This combination of θ_L^{bn} and θ_V^{bn} coincides with a broad minimum in χ^2 for all the `BNtorus` model fits and is within 1σ of the IR-based half-opening and viewing angles. The `MYtorus` model constraints are similar, though weaker. The X-ray and infrared torus models are thus both consistent with scenarios where the line-of-sight viewing angle is close to the half-opening angle. The data do not favor extreme geometries, such as edge-on viewing angle, or tori that are disk-like ($\theta_L^{bn} \rightarrow 90°$) or sphere-like ($\theta_L^{bn} \rightarrow 0°$). This "skimming" of the edge of the torus by the line-of-sight viewing angle suggests that, had IRAS 09104+4109 been viewed at a viewing angle smaller by only a few degrees, it would have been classified as a broad-line object in direct light.

5. The constraints on the bolometric luminosity of IRAS 09104+4109 from the X-ray and infrared data are also consistent with each other. The intrinsic 2–10 keV luminosity lies in the range of $(1-2) \times 10^{45}$ erg s^{-1}. Assuming a bolometric correction of 50–130 leads to an estimate of $L_{bol} \sim (0.5-2.5) \times 10^{47}$ erg s^{-1}. Instead starting from the intrinsic AGN luminosity derived from IR modeling, and assuming that 30% of the bolometric emission emerges in the infrared, yields $\sim 1.8 \times 10^{47}$ erg s^{-1}.

6. The detection of high-excitation iron lines in the optical spectrum provides further constraints on the geometry of the AGN obscurer. If these lines arise in a CLR, then their detection is consistent with a line of sight that skims the torus—the CLR is visible in direct light, but the BLR can only be seen in scattered light. Taking the distance constraints from the

detection of [Fe X] $\lambda 6374$ but not [Fe XIV] $\lambda 5303$ then places the bulk of the dust column that composes the IR-emitting torus to within a vertical height of 20 pc of the nucleus. The X-ray obscurer is thus plausibly within this distance, also. Assuming that the geometry of the infrared model is correct then places the outer "edge" of the IR-emitting torus within 125 pc of the nucleus and the inner edge within 2 pc. These values have large systematic uncertainties that are difficult to estimate, and are based on the aforementioned combining of assumptions across disparate models.

7. The joint X-ray data set, despite its broadband coverage, is insufficient to provide constraints on the AGN torus geometry without keeping some model parameters fixed, and/or without constraints from the infrared and optical data. The 15 ks *NuSTAR* observation, despite the $\simeq 13\sigma$ detection above 10 keV, does not constrain the AGN spectrum of IRAS 09104+4109 substantially better than the archival data below 10 keV. The joint X-ray data set gives less of a χ^2 gradient toward hard photon indices; however, similar solutions can be found from the archival data alone, albeit with larger uncertainties. Moreover, both θ_L^{bn} and θ_V^{bn} cannot be independently constrained. Despite its coverage above 10 keV, the current *NuSTAR* data are not of sufficient quality to uniquely constrain the AGN spectrum, so the fits remain susceptible to assumptions. A longer *NuSTAR* observation of IRAS 09104+4109 is essential for constraining the structure of the torus directly from the X-ray band.

REFERENCES

Alatalo, K., Lacy, M., Lanz, L., et al. 2015, ApJ, 798, 31
Alexander, D. M., Bauer, F. E., Chapman, S. C., et al. 2005, ApJ, 632, 736
Alexander, D. M., & Hickox, R. C. 2012, NewAR, 56, 93
Annuar, A., Gandhi, P., Alexander, D. M., et al. 2015, ApJ, 815, 36
Arévalo, P., Bauer, F. E., Puccetti, S., et al. 2014, ApJ, 791, 81
Armus, L., Soifer, B. T., & Neugebauer, G. 1999, Ap&SS, 266, 113
Arnaud, K. A. 1996, in ASP Conf. Ser. 101, Astronomical Data Analysis Software and Systems V XSPEC: The First Ten Years, ed. G. H. Jacoby & J. Barnes (San Francisco, CA: ASP), 17
Asmus, D., Gandhi, P., Hönig, S. F., et al. 2015, MNRAS, 454, 766
Baloković, M., et al. 2016, ApJ, submitted
Baldwin, J. A., Phillips, M. M., & Terlevich, R. 1981, PASP, 93, 5
Balog, Z., Müller, T., Nielbock, M., et al. 2014, ExA, 37, 129
Baloković, M., Comastri, A., Harrison, F. A., et al. 2014, ApJ, 794, 111
Bauer, F. E., Arévalo, P., Walton, D. J., et al. 2015, ApJ, 812, 116
Béthermin, M., Le Floc'h, E., Ilbert, O., et al. 2012, A&A, 542, A58
Bildfell, C., Hoekstra, H., Babul, A., & Mahdavi, A. 2008, MNRAS, 389, 1637
Bridge, C. R., Blain, A., Borys, C. J. K., et al. 2013, ApJ, 769, 91
Brightman, M., Baloković, M., Stern, D., et al. 2015, ApJ, 805, 41
Brightman, M., & Nandra, K. 2011, MNRAS, 413, 1206
Brown, J. C., & McLean, I. S. 1977, A&A, 57, 141
Bruzual, G., & Charlot, S. 2003, MNRAS, 344, 1000
Burgarella, D., Buat, V., Gruppioni, C., et al. 2013, A&A, 554, A70
Burtscher, L., Meisenheimer, K., Tristram, K. R. W., et al. 2013, A&A, 558, A149
Casey, C. M., Narayanan, D., & Cooray, A. 2014, PhR, 541, 45
Chapman, S. C., Blain, A. W., Smail, I., & Ivison, R. J. 2005, ApJ, 622, 772
Chiang, C.-H., Cackett, E. M., Gandhi, P., & Fabian, A. C. 2013, MNRAS, 430, 2943
Chung, A., Yun, M. S., Naraynan, G., Heyer, M., & Erickson, N. R. 2011, ApJL, 732, L15
Combes, F., García-Burillo, S., Braine, J., et al. 2011, A&A, 528, A124
Crawford, C. S., & Vanderriest, C. 1996, MNRAS, 283, 1003
Croton, D. J., Springel, V., White, S. D. M., et al. 2006, MNRAS, 365, 11
Cutri, R. M., Wright, E. L., Conrow, T., et al. 2013, Explanatory Supplement to the AllWISE Data Release Products (Washington, D.C.: NASA)
Dadina, M. 2008, A&A, 485, 417
Deane, J. R., & Trentham, N. 2001, MNRAS, 326, 1467
Del Moro, A., Mullaney, J. M., Alexander, D. M., et al. 2014, ApJ, 786, 16
Delvecchio, I., Gruppioni, C., Pozzi, F., et al. 2014, MNRAS, 439, 2736
Dickinson, M., Papovich, C., Ferguson, H. C., & Budavári, T. 2003, ApJ, 587, 25
Efstathiou, A. 2006, MNRAS, 371, L70
Efstathiou, A., Christopher, N., Verma, A., & Siebenmorgen, R. 2013, MNRAS, 436, 1873
Efstathiou, A., Pearson, C., Farrah, D., et al. 2014, MNRAS, 437, L16
Efstathiou, A., & Rowan-Robinson, M. 1990, MNRAS, 245, 275
Efstathiou, A., & Rowan-Robinson, M. 1995, MNRAS, 273, 649
Efstathiou, A., Rowan-Robinson, M., & Siebenmorgen, R. 2000, MNRAS, 313, 734
Efstathiou, A., & Siebenmorgen, R. 2009, A&A, 502, 541
Evans, A. S., Sanders, D. B., Cutri, R. M., et al. 1998, ApJ, 506, 205
Fabian, A. C. 2012, ARA&A, 50, 455
Fabian, A. C., & Crawford, C. S. 1995, MNRAS, 274, L63
Fabian, A. C., Shioya, Y., Iwasawa, K., et al. 1994, ApJL, 436, L51
Farrah, D., Afonso, J., Efstathiou, A., et al. 2003, MNRAS, 343, 585
Farrah, D., Geach, J., Fox, M., et al. 2004, MNRAS, 349, 518
Farrah, D., Lebouteiller, V., Spoon, H. W. W., et al. 2013, ApJ, 776, 38
Farrah, D., Lonsdale, C. J., Weedman, D. W., et al. 2008, ApJ, 677, 957
Farrah, D., Serjeant, S., Efstathiou, A., Rowan-Robinson, M., & Verma, A. 2002, MNRAS, 335, 1163
Farrah, D., Surace, J. A., Veilleux, S., Sanders, D. B., & Vacca, W. D. 2005, ApJ, 626, 70
Farrah, D., Urrutia, T., Lacy, M., et al. 2012, ApJ, 745, 178
Fazio, G. G., Hora, J. L., Allen, L. E., et al. 2004, ApJS, 154, 10
Ferguson, J. W., Korista, K. T., & Ferland, G. J. 1997, ApJS, 110, 287
Franceschini, A., Bassani, L., Cappi, M., et al. 2000, A&A, 353, 910

Gaibler, V., Khochfar, S., Krause, M., & Silk, J. 2012, MNRAS, 425, 438
Gandhi, P., Horst, H., Smette, A., et al. 2009, A&A, 502, 457
Gandhi, P., Lansbury, G. B., Alexander, D. M., et al. 2014, ApJ, 794, 176
Gelbord, J. M., Mullaney, J. R., & Ward, M. J. 2009, MNRAS, 397, 172
Genzel, R., Lutz, D., Sturm, E., et al. 1998, ApJ, 498, 579
Griffin, M. J., Abergel, A., Abreu, A., et al. 2010, A&A, 518, L3
Gruppioni, C., Berta, S., Spinoglio, L., et al. 2016, MNRAS, 458, 4297
Hall, P. B., Ellingson, E., & Green, R. F. 1997, AJ, 113, 1179
Han, Y., & Han, Z. 2012, ApJ, 749, 123
Harris, K., Farrah, D., Schulz, B., et al. 2016, MNRAS, 457, 4179
Harrison, F. A., Craig, W. W., Christensen, F. E., et al. 2013, ApJ, 770, 103
Hernán-Caballero, A., Caballero, A., Pérez-Fournon, I., et al. 2009, MNRAS, 395, 1695
Hewett, P. C., & Wild, V. 2010, MNRAS, 405, 2302
Hines, D. C., Schmidt, G. D., Wills, B. J., Smith, P. S., & Sowinski, L. G. 1999, ApJ, 512, 145
Hines, D. C., & Wills, B. J. 1993, ApJ, 415, 82
Hlavacek-Larrondo, J., Fabian, A. C., Edge, A. C., et al. 2012, MNRAS, 421, 1360
Houck, J. R., Roellig, T. L., van Cleve, J., et al. 2004, ApJS, 154, 18
Iglesias-Páramo, J., Buat, V., Hernández-Fernández, J., et al. 2007, ApJ, 670, 279
Ishibashi, W., & Fabian, A. C. 2012, MNRAS, 427, 2998
Iwasawa, K., Crawford, C. S., Fabian, A. C., & Wilman, R. J. 2005, MNRAS, 362, L20
Iwasawa, K., Fabian, A. C., & Ettori, S. 2001, MNRAS, 321, 15
Kalberla, P. M., Burton, W. B., Hartmann, D., et al. 2005, A&A, 440, 775
Kewley, L. J., Heisler, C. A., Dopita, M. A., & Lumsden, S. 2001, ApJS, 132, 37
King, A. 2005, ApJL, 635, L121
Kleinmann, S. G., Hamilton, D., Keel, W. C., et al. 1988, ApJ, 328, 161
Korista, K. T., & Ferland, G. J. 1989, ApJ, 343, 678
Koss, M. J., Romero-Cañizales, C., Baronchelli, L., et al. 2015, ApJ, 807, 149
Lagache, G., Puget, J.-L., & Dole, H. 2005, ARA&A, 43, 727
LaMassa, S. M., Yaqoob, T., Ptak, A. F., et al. 2014, ApJ, 787, 61
Lansbury, G. B., Alexander, D. M., Del Moro, A., et al. 2014, ApJ, 785, 17
Lansbury, G. B., Gandhi, P., Alexander, D. M., et al. 2015, ApJ, 809, 115
Lanzuisi, G., Perna, M., Delvecchio, I., et al. 2015, A&A, 578, A120
Lebouteiller, V., Barry, D. J., Spoon, H. W. W., et al. 2011, ApJS, 196, 8
Liedahl, D. A., Osterheld, A. L., & Goldstein, W. H. 1995, ApJL, 438, L115
Lilly, S. J., Le Fevre, O., Hammer, F., & Crampton, D. 1996, ApJL, 460, L1
Lonsdale, C. J., Farrah, D., & Smith, H. E. 2006, in Astrophysics Update 2, ed. J. W. Mason (Chichester: Praxis), 285
Lusso, E., Comastri, A., Simmons, B. D., et al. 2012, MNRAS, 425, 623
Madau, P., & Dickinson, M. 2014, ARA&A, 52, 415
Madsen, K. K., Harrison, F. A., Markwardt, C. B., et al. 2015, ApJS, 220, 8
Magdziarz, P., & Zdziarski, A. A. 1995, MNRAS, 273, 837
Magorrian, J., Tremaine, S., Richstone, D., et al. 1998, AJ, 115, 2285
Malizia, A., Molina, M., Bassani, L., et al. 2014, ApJ, 782, 25
Marconi, A., Risaliti, G., Gilli, R., et al. 2004, MNRAS, 351, 169
Massey, P., & Gronwall, C. 1990, ApJ, 358, 344
McDonald, M., McNamara, B. R., van Weeren, R. J., et al. 2015, ApJ, 811, 111
Mewe, R., Gronenschild, E. H. B. M., & van den Oord, G. H. J. 1985, A&AS, 62, 197
Mignoli, M., Vignali, C., Gilli, R., et al. 2013, A&A, 556, A29
Murayama, T., & Taniguchi, Y. 1998, ApJL, 497, L9
Murphy, K. D., & Yaqoob, T. 2009, MNRAS, 397, 1549
Neugebauer, G., Habing, H. J., van Duinen, R., et al. 1984, ApJL, 278, L1
Oke, J. B., & Gunn, J. E. 1982, PASP, 94, 586
Osterbrock, D. E. 1981, ApJ, 246, 696
O'Sullivan, E., Giacintucci, S., Babul, A., et al. 2012, MNRAS, 424, 2971
Ott, S. 2010, in ASP Conf. Series 434, Astronomical Data Analysis Software and Systems XIX, ed. Y. Mizumoto, K.-I. Morita, & M. Ohishi (San Fransisco, CA: ASP), 139
Penston, M. V., Fosbury, R. A. E., Boksenberg, A., Ward, M. J., & Wilson, A. S. 1984, MNRAS, 208, 347
Pérez-González, P. G., Rieke, G. H., Egami, E., et al. 2005, ApJ, 630, 82
Perri, M., Puccetti, S., Spagnuolo, N., et al. 2014, The NuSTAR Data Analysis Software Guide (Washington, D.C.: NASA), http://heasarc.gsfc.nasa.gov/docs/nustar/analysis/nustar_swguide.pdf
Piconcelli, E., Fiore, F., Nicastro, F., et al. 2007, A&A, 473, 85
Pilbratt, G. L., Riedinger, J. R., Passvogel, T., et al. 2010, A&A, 518, L1
Pipino, A., Kaviraj, S., Bildfell, C., et al. 2009, MNRAS, 395, 462
Poglitsch, A., Waelkens, C., Geis, N., et al. 2010, A&A, 518, L2

Puccetti, S., Comastri, A., Fiore, F., et al. 2014, ApJ, 793, 26
Reynolds, C. S., Ward, M. J., Fabian, A. C., & Celotti, A. 1997, MNRAS, 291, 403
Richards, G. T., Strauss, M. A., Fan, X., et al. 2006, AJ, 131, 2766
Risaliti, G., & Elvis, M. 2004, in Supermassive Black Holes in the Distant Universe Vol. 308, ed. A. J. Barger (Dordrecht: Kluwer), 187
Rivers, E., Markowitz, A., & Rotschild, R. 2013, ApJ, 772, 114
Rose, M., Elvis, M., & Tadhunter, C. N. 2015, MNRAS, 448, 2900
Rowan-Robinson, M. 2000, MNRAS, 316, 885
Rowan-Robinson, M., Oliver, S., Wang, L., et al. 2016, MNRAS, in press (arXiv:1605.03937)
Rowan-Robinson, M., & Wang, L. 2010, MNRAS, 406, 720
Ruiz, A., Miniutti, G., Panessa, F., & Carrera, F. J. 2010, A&A, 515, A99
Ruiz, A., Risaliti, G., Nardini, E., Panessa, F., & Carrera, F. J. 2013, A&A, 549, A125
Russell, H. R., Fabian, A. C., Sanders, J. S., et al. 2010, MNRAS, 402, 1561
Sargsyan, L., Mickaelian, A., Weedman, D., & Houck, J. 2008, ApJ, 683, 114
Schaye, J., Crain, R. A., Bower, R. G., et al. 2015, MNRAS, 446, 521
Shan, H. G., & Chen, P. S. 2012, MNRAS, 421, 235
Shirazi, M., & Brinchmann, J. 2012, MNRAS, 421, 1043
Silk, J. 2013, ApJ, 772, 112
Soifer, B. T., Neugebauer, G., Armus, L., & Shupe, D. L. 1996, AJ, 111, 649
Stasińska, G., Cid Fernandes, R., Mateus, A., Sodré, L., & Asari, N. V. 2006, MNRAS, 371, 972
Stern, D. 2015, ApJ, 807, 129
Stern, D., Lansbury, G. B., Assef, R. J., et al. 2014, ApJ, 794, 102
Taniguchi, Y., Sato, Y., Kawara, K., Murayama, T., & Mouri, H. 1997, A&A, 318, L1
Tran, H. D., Cohen, M. H., & Villar-Martin, M. 2000, AJ, 120, 562
Tremaine, S., Gebhardt, K., Bender, R., et al. 2002, ApJ, 574, 740
Vasudevan, R. V., & Fabian, A. C. 2007, MNRAS, 381, 1235
Verma, A., Rowan-Robinson, M., McMahon, R., & Efstathiou, A. 2002, MNRAS, 335, 574
Véron-Cetty, M.-P., & Véron, P. 2006, A&A, 455, 773
Vignali, C., Mignoli, M., Gilli, R., et al. 2014, A&A, 571, A34
Vignali, C., Piconcelli, E., Lanzuisi, G., et al. 2011, MNRAS, 416, 2068
Wang, L., Farrah, D., Oliver, S. J., et al. 2013, MNRAS, 431, 648
Wang, L., & Rowan-Robinson, M. 2010, MNRAS, 401, 35
Werner, M. W., Roellig, T. L., Low, F. J., et al. 2004, ApJS, 154, 1
Wright, E. L., Eisenhardt, P. R. M., Mainzer, A. K., et al. 2010, AJ, 140, 1868
Wuyts, S., Förster Schreiber, N. M., van der Wel, A., et al. 2011, ApJ, 742, 96
Yaqoob, T. 2012, MNRAS, 423, 3360
Zakamska, N. L., Gómez, L., Strauss, M. A., & Krolik, J. H. 2008, AJ, 136, 1607
Zubovas, K., Nayakshin, S., King, A., & Wilkinson, M. 2013, MNRAS, 433, 3079